Solution-processed Visible-blind UV-A Photodetectors Based on $CH_3NH_3PbCl_3$ Perovskite Thin Films

Erjin Zheng

A thesis

submitted in partial fulfillment of the

requirements for the degree of

Master of Science in Chemical Engineering

University of Washington

2017

Reading Committee:

Qiuming Yu, Chair

Vincent C. Holmberg

Program Authorized to Offer Degree:

Chemical Engineering

University of Washington

Abstract

Solution-processed Visible-blind UV-A Photodetectors Based on $CH_3NH_3PbCl_3$ Perovskite Thin Films

Erjin Zheng

Chair of the Supervisory Committee:
Research Professor Qiuming Yu
Department of Chemical Engineering

In this work, methylammonium lead trichloride ($CH_3NH_3PbCl_3$) perovskite thin films were fabricated via a two-step spin coating and solvent-vapor-assisted thermal annealing method under low temperature. The films exhibited cubic crystalline structure and pinhole-free morphologies. The possible charge traps were investigated via the analysis of photoluminescence (PL) spectra of perovskite films prepared with different lead chloride ($PbCl_2$) precursor concentrations while maintaining the same concentration of methylammonium chloride (CH_3NH_3Cl). Prototypical ultraviolet (UV) photodetectors with the structure of ITO/$CH_3NH_3PbCl_3$/Poly (triaryl amine) (PTAA)/Al were fabricated and showed low dark current density 1.60×10^{-5} mA/cm^2 under -1 V reverse bias, strong photoresponse in 300-400 nm region, and a high UV-visible rejection ratio up

to 500 under 0 or -0.5 V bias. All the results demonstrated that low-temperature solution-processed $CH_3NH_3PbCl_3$ perovskite thin films offer a great potential for making flexible, lightweight visible-blind UV-A photodetectors.

TABLE OF CONTENTS

LIST OF FIGURES

ACKNOWLEDGEMENTS

The author expresses sincere appreciation to his advisor Professor Qiuming Yu for her guidance and encouragement, his group members Beau Richardson, David Galvan, Monica Esopi, Gabriella Tosado, Beiying Zhou, Chao Hou, and Brian Yuh for their ideas, and his parents and wife Yishu Yang for their invaluable support.

Chapter 1. INTRODUCTION

This paper has been published in Journal of Materials Chemistry C by Erjin Zheng, Brian Yuh, Gabriella A. Tosado, and Qiuming Yu*, with the title "Solution-processed Visible-blind UV-A Photodetectors Based on $CH_3NH_3PbCl_3$ Perovskite Thin Films" (*J. Mater. Chem. C, 2017, 5, 3796*).

1.1 PEROVSKITE

Hybrid organic-inorganic perovskites have recently gained tremendous attention as they have enabled bright, widely tunable light-emitting diodes,[1, 2] photodetector with high detectivity,[3] as well as solar cells that have reached certified power conversion efficiency (PCE) to 22.1%.[4] The attractive optical and electronic properties of hybrid organic-inorganic perovskites include high light absorption coefficients,[5] direct band gaps,[6] long and balanced carrier diffusion lengths,[7] and high carrier mobilities.[8] The low temperature solution processibility enables low-cost, large-area fabrication to make flexible, lightweight devices.[9] The spectral response and the valence and conduction band positions of perovskites can be tuned via the choice of group IVa cation (Pb^{2+}, Sn^{2+}) and halide anion (I^-, Br^-, Cl^-).[10-14] The band gap of methylammonium lead-tin triiodide ($CH_3NH_3Sn_xPb_{1-x}I_3$) has been demonstrated to vary from 1.55 to 1.17 eV by varying x from 0 to 0.5 and 0.75, and then to 1.30 eV when x is further increased to 1.[10] The band gap of $CH_3NH_3PbX_3$ is increased from 1.55 eV for $CH_3NH_3PbI_3$ to 2.39 eV for $CH_3NH_3PbBr_3$ and to 3.17 eV for $CH_3NH_3PbCl_3$[11, 12] due to the stronger covalent interaction between halide anion and Pb^{2+} cation as the halide anion changes from I^- to Br^- and Cl^-.[13, 14]

1.2 PEROVSKITE PHOTODETECTORS

Hybrid organic-inorganic perovskites have been applied to make photodetectors with the prototypes that are roughly divided into two sub-categories: vertically stacked photodiode-type detectors,[3, 15-20] and laterally structured phototransistor-type detectors.[21-28] While these photodetectors utilized different polycrystalline thin film or nanowire perovskites as the light absorbing layer, all of them have demonstrated the detection of photons up to visible or near infrared wavelengths. The detection of ultraviolet (UV) light has a wide range of applications, such as chemical, environmental and biological analysis and monitoring, flame and radiation detection, astronomical studies, and optical communications. Development of UV photodetectors has drawn extensive attention.[29, 30] UV light is typically divided into four spectral regions from 400 to 10 nm: UV-A (400 to 320 nm), UV-B (320 to 280 nm), UV-C (280 to 200 nm), and far UV (200 to 10 nm).[29, 30] As visible light covers the range of wavelengths from 400 to 700 nm, UV photodetectors that have higher sensitivity to the radiation below 400 nm than above 400 nm are called 'visible-blind'. Methylammonium lead chloride ($CH_3NH_3PbCl_3$) as a wide-bandgap perovskite shows a high optical absorption coefficient in UV-A range (320 to 400 nm) while transparent to visible light,[11, 12] which makes it a promising candidate for visible-blind UV-A photodetectors.

1.3 UV-A PHOTODETECTOR BASED ON METHYLAMMONIUM LEAD TRICHLORIDE PEROVSKITE

Recently, a few UV photodetectors based on $CH_3NH_3PbCl_3$ perovskite have been reported. Maculan *et al*. applied inverse temperature crystallization method to grow bulk $CH_3NH_3PbCl_3$ single crystals and built the UV photodetectors by polishing the single crystals to the thickness of 350 μm, and coating 20 nm Pt on one side as the transparent anode and 25 nm Ti and 100 nm Au on

the other side as the cathode. The device exhibits a responsivity of 46.9 mA/W and detectivity of 1.2×10^{10} Jones when illuminated by a 365 nm wavelength light with the intensity of 1 W/cm^2 and under a 15 V bias.[31] Fang *et al*. sandwiched a $CH_3NH_3PbCl_3$ single crystal about 1 mm thick, made by precipitating supersaturated precursor solution, between Ga and a thermally evaporated 20 nm Au electrode to build a photodetector device. The device exhibited narrow spectral response with a full-width at half-maximum (FWHM) of < 20 nm centered at around 420 nm. The narrow spectral band was achieved by surface-charge recombination-induced suppression of charge collection for short-wavelength excitation. The external quantum efficiency (EQE) was low (0.2% ~ 1.6%) because of the low transparency of the 25 nm Au electrode and no other device performance data was reported.[32] Wang *et al.* reported phototransistor-type UV photodetectors by making $CH_3NH_3PbCl_3$ polycrystalline thin films on 50 nm thick, patterned Au electrodes with 5 μm gaps. The $CH_3NH_3PbCl_3$ polycrystalline thin films were fabricated by thermal evaporation of lead chloride ($PbCl_2$) thin layer followed by spin coating of methylammonium chloride (CH_3NH_3Cl) and annealing. The devices showed a responsivity of 7.56 A/W to 360 nm wavelength light with the intensity of 0.1 mW/cm^2 and under a 4 V bias.[33] Adinolfi *et al.* utilized a modified inverse temperature crystallization method to grow $CH_3NH_3PbCl_3$ single crystals that can cover the 5 μm gap between patterned ITO electrodes on glass to realize laterally structured phototransistor-type UV photodetectors. The devices demonstrated a very high responsivity of 18 A/W and detectivity of 10^{12} Jones under 385 nm wavelength light with 4 nW intensity under a 5 V bias.[34] As aforementioned, many studies have been reported on vertically stacked photodiode-type detectors based on solution-processed perovskite polycrystalline thin films in the visible light range,[3, 15-20] and demonstrated attractive device performance such as ultrahigh gain ~489 and high responsivity ~242 A/W,[15] high detectivity ~10^{14} Jones,[3] and low dark current density ~10^{-9} A/cm^2 under a -1 V

reverse bias.[16] There is no report on UV photodetectors with the vertically stacked photodiode-type architecture using solution-processed $CH_3NH_3PbCl_3$ polycrystalline thin films, which could be partly due to the difficulty involved when fabricating high quality $CH_3NH_3PbCl_3$ polycrystalline thin films.[11, 12]

In this thesis, we reported a two-step solution process, low-temperature solvent-vapor-assisted thermal annealing method to fabricate uniform, pinhole-free $CH_3NH_3PbCl_3$ thin films and its implication in UV photodetectors with a simple photodiode device structure of ITO/$CH_3NH_3PbCl_3$/Poly (triaryl amine) (PTAA)/Al. The fabricated films exhibited high crystallinity with a cubic phase and a sharp absorption cutoff at the frontage of UV-A range (400 nm). The possible traps were investigated via the analysis of photoluminescence (PL) spectra of perovskite films prepared with different $PbCl_2$ precursor concentrations. Prototypical devices in photodiode structure based on trap-reduced $CH_3NH_3PbCl_3$ thin films were fabricated and showed a photoresponse in the 300-400 nm region and a high UV-visible rejection ratio up to 500. All the results demonstrated that low-temperature solution-processed $CH_3NH_3PbCl_3$ thin films could be a promising candidate for making flexible, lightweight visible-blind UV-A photodetectors.

Chapter 2. EXPERIMENTAL METHODS

2.1 Methylammonium Chloride Synthesis

CH_3NH_3Cl was synthesized by a modified procedure based on methods reported previously.[31] Specifically, 22 mL of methylamine (33 wt % in absolute ethanol, Sigma Aldrich) were charged with 100 mL ethanol (anhydrous, ≥ 99.5%, Sigma Aldrich) in a 250 mL round bottom flask. The solution was stirred in an ice bath under nitrogen protection. 12 mL of hydrochloride acid (37 wt % in water, Sigma Aldrich) were then added dropwise to the methylamine solution over 30 min. The resulting mixture was stirred under 0 °C for 2 h. The white precipitate was recovered by rotary evaporation at 40 °C, then dissolved in ethanol followed by sedimentation in diethyl ether (anhydrous, Fisher Scientific) by stirring the solution for 30 min. The mixture was then washed three times with diethyl ether. The precipitated solid was collected and dried under 50 °C in a vacuum oven for 24 h.

2.2 Methylammonium Lead Trichloride Bulk Crystal Growth

Bulk crystal was grown by inverse temperature crystallization method as reported previously with slight modification.[31] A 1 M $CH_3NH_3PbCl_3$ precursor solution was prepared by dissolving equal mole CH_3NH_3Cl and $PbCl_2$ in DMSO-DMF (1:1 by volume). The solution was then filtered using a PTFE filter with 0.2 μm pore size. The solution was sealed in a 10 mL vial and kept undisturbed for 1 h under 85 °C. The small crystals were kept as seeds. The same procedure was repeated by adding seeds to grow large crystals.

2.3 Methylammonium Lead Trichloride Thin Film Fabrication

To fabricate $CH_3NH_3PbCl_3$ thin films, lead chloride ($PbCl_2$, 99.999%, Sigma Aldrich) and synthesized CH_3NH_3Cl were dissolved in dimethyl sulfoxide (DMSO, anhydrous, ≥99.9%, Sigma Aldrich) and 2-propanol (anhydrous, 99.5%, Sigma Aldrich) to form 350 mg/mL and 20 mg/mL solutions, respectively, under 70 °C in a nitrogen filled glovebox. CH_3NH_3Cl solution was filtered through a 0.2 μm PTFE filter before use. Substrates (plain glass or ITO coated glass with sheet resistance = 10 Ω sq^{-1}, Colorado Concept Coatings LLC) were first cut into 15 mm × 15 mm pieces, then cleaned sequentially by sonication in soapy millipore deionized water, millipore deionized water, acetone, and isopropanol each for 15 min and then treated with oxygen plasma for 10 min and transferred into glovebox. A drop of 70 μL $PbCl_2$ solution was first spin coated onto a substrate at 6000 rpm for 30 s and annealed at 70 °C for 10 min. A drop of 70 μL of CH_3NH_3Cl solution was then quickly spin coated onto the $PbCl_2$ film at 4000 rpm for 30 s and annealed at 70 °C for 30 min. For thermal-only annealing, the substrates were transferred onto a hotplate at 100 °C and annealed for 1 h. For solvent-assisted thermal annealing, the substrates were transferred onto a hotplate at 100 °C and covered by a glass petri dish. A drop of 10 μL DMSO was added onto the hotplate inside petri dish and annealed for 1 h. $CH_3NH_3PbCl_3$ thin films were also made with the $PbCl_2$ concentrations of 250, 300, and 450 mg/mL to vary the ratio of $PbCl_2$ to CH_3NH_3Cl.

Besides the optimized fabrication method, one-step spin coating followed by thermal annealing and solvent-vapor-assisted thermal annealing, and one-step spin coating with nano-pinning followed by thermal annealing and solvent-vapor-assisted annealing were also attempted as described below.

One-step spin coating: Equal mole CH_3NH_3Cl and $PbCl_2$ were dissolved in DMSO-DMF (1:1 by volume) to get a 1 M $CH_3NH_3PbCl_3$ precursor solution. The precursor was stirred for 12 h at 70

°C and filtered by a 0.2 μm PTFE filter. 100 μL of precursor was added onto a 15 mm × 15 mm substrate and spin coated at 4000 rpm for 60 s. For thermal annealing, substrates were heated on a hotplate at 70 °C for 60 min. For DMSO-vapor-assisted thermal annealing, substrates were first heated on a hotplate at 70 °C for 60 min. Then the substrates were covered with a glass petri dish on the hotplate, 10 μL of DMSO was added from the edge of the petri dish and heated at 70 °C for 60 min.

Nano-pinning: Precursor solution was prepared as described above. 100 μL of precursor solution was added onto a 15 mm × 15 mm substrate. Nano-pinning method was performed as reported previously with slight modification.[7] Two spin speeds were applied to perform nano-pinning: 500 rpm for 10 s and then 3000 rpm for 90 s. When 70 s passed, 100 μL of toluene or chloroform was added on the substrate in less than 2 s. For thermal annealing, substrates were heated on a hotplate at 70 °C for 10 min. For DMSO-vapor-assisted thermal annealing, substrates were first heated on a hotplate at 70 °C for 10 min. Then the substrates were covered with a glass petri dish on the hotplate, 10 μL of DMSO was added from the edge of the petri dish and heated at 70 °C for 60 min.

2.4 Film Characterization

Scanning electron microscopy (SEM) measurements were carried out on an FEI Sirion SEM to investigate the surface morphology of the thin films. Two-dimensional X-ray diffraction (XRD) measurements were performed on a Bruker GADDS D8 Discover diffractometer using Cu Kα radiation (λ = 1.5419 Å) to study the crystalline structures of the precursor and perovskite films. Data was processed using the EVA package provided by Bruker Axs. UV-Vis absorption and photoluminescence (PL) spectra of perovskite thin films were collected via a Varian Cary 5000

UV-Vis-NIR spectrophotometer and a Horiba Fluorolog 3 Spectrofluorometer, respectively. Film thicknesses were measured using a KLA Tencor Alpha-Step 500 Profiler.

2.5 Device Fabrication

The $CH_3NH_3PbCl_3$ films on ITO coated glass substrates were fabricated as described above. After the substrates were cooled down to room temperature, a drop of 70 μL of 10 mg/mL Poly (triaryl amine) (PTAA, MW = 15-25 KDa, Solaris Chem Inc.) toluene solution was spin coated onto a $CH_3NH_3PbCl_3$ thin film at 3000 rpm for 30 s, followed by annealing at 100 °C for 10 min. Devices were finished by thermal deposition of 100 nm aluminum layer at the rate of 0.2 nm/s in a background vacuum less than 2×10^{-6} Torr. The resulting devices have a structure of ITO/$CH_3NH_3PbCl_3$/PTAA/Al. The working area of devices for monochromatic illumination and EQE measurements is 0.057 cm^2, and for the illumination by solar simulator is 0.1 cm^2.

2.6 Device Characterization

The devices were characterized under dynamic vacuum in a custom built vacuum chamber fitted with electrical leads. White light from a 75 W xenon arc lamp (Newport Co., Oriel PhotoMax) was filtered by a grating monochromator (Acton Research Co., SpectraPro-2150i) to achieve a bandpass of ~3 nm (FWHM) for the incident CW probe light. The current density-voltage (J-V) characteristics under dark and 360 nm illumination with the intensity of 0.267 mW/cm^2 were recorded using a Keithley 2400 with a scan step of 10 mV from +1 V to -1 V and current values were averaged from 10 points under each bias with a delay time of 10 ms. The external quantum efficiency (EQE) was recorded with a wavelength step of 2 nm/s and current values were averaged from 20 points with a delay time of 10 ms. The J-V characteristics were also measured by a Keithley 2400 under AM 1.5 G of simulated solar light with an illuminated

intensity of 100 mW/cm^2 calibrated by employing a standard Si photodiode detector equipped with KG-5 filter. The devices were scanned from +1 V to -1 V with voltage step and time interval of 4 mV and 10 ms, respectively.

Chapter 3. RESULT AND DISCUSSION

3.1 METHYLAMMONIUM LEAD TRICHLORIDE THIN FILM FABRICATION

Perovskites thin films have been typically made via one-step or two-step solution processes. One-step solution process was firstly applied to fabricate perovskite thin films by spin coating a solution containing all precursors followed by thermal annealing. While noncontinious perovskite films were frequently observed using lead iodide (PbI_2) and methyl ammonium halide (CH_3NH_3X) blend solutions, which might be related to the interaction of perovskite with a substrate surface,[35, 36] it may also be due to the low viscosity of the perovskite solution and the quick crystallization of the mixed precursor upon drying the spun films.[37] Nano-pinning method were then developed based on the one-step spin coating technique by introducing toluene or chloroform during spin coating to wash out "good" solvent such as DMSO. The $CH_3NH_3PbBr_3$ thin films made with the nano-pinning method exhibited flat and uniform morphologies.[38] Two-step solution spin coating method, also known as an interdiffusion method, has been further developed to form continuous, compact iodine perovskite films for solar cell applications.[9] By spin coating precursor stacking layers of PbI_2 and methylammonium iodide (CH_3NH_3I), methylammonium cations diffuse into the PbI_2 layer to form perovskites during thermal annealing. Later on, it was reported that a solvent-vapor-assisted thermal annealing can effectively increase the perovskite grain size and crystallinity, resulting in a significant improvement in material electronic properties and a great enhancement in photovoltaic device performance.[39, 40]

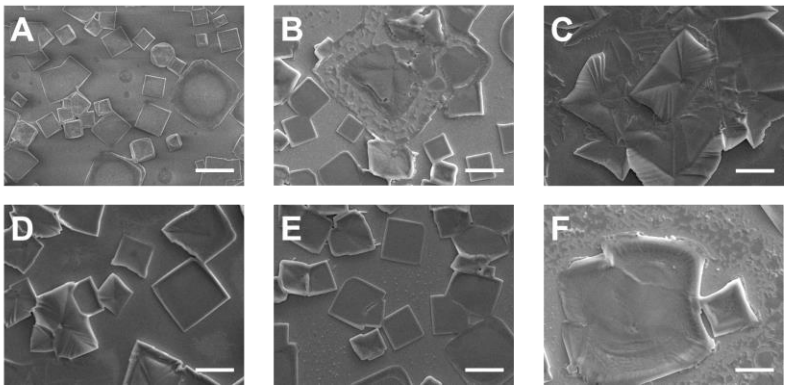

Figure 3.1. SEM images of $CH_3NH_3PbCl_3$ thin film fabricated via (A) one-step spin coating with thermal annealing, (B) one-step spin coating with DMSO-vapor-assisted thermal annealing, (C) nano-pinning with chloroform followed by thermal annealing, (D) nano-pinning with toluene followed by thermal annealing, (E) nano-pinning with chloroform followed by DMSO-vapor-assisted thermal annealing and (F) nano-pinning with toluene followed by DMSO-vapor-assisted thermal annealing. Scale bar: 10 μm.

We fabricated $CH_3NH_3PbCl_3$ thin films using both one-step and two-step solution process methods. We used different one-step solution process methods, including one-step spin coating followed by thermal annealing and solvent-vapor-assisted thermal annealing, and one-step spin coating with nano-pinning followed by thermal annealing and solvent-vapor-assisted annealing (See Experimental Method section for details). All films exhibited rough, nonuniform surfaces with many large size cuboids as shown in Fig. 3.1.

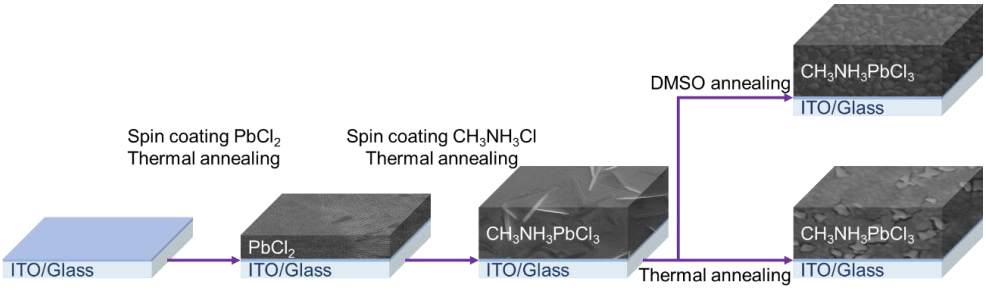

Figure 3.2. Schematic illustration of two-step solution process method for making $CH_3NH_3PbCl_3$ thin films.

We further applied the two-step solution process method followed by thermal annealing and solvent-vapor-assisted thermal annealing under different temperatures to fabricate $CH_3NH_3PbCl_3$ thin films as illustrated in Fig. 3.2. A $PbCl_2$ DMSO solution with the concentration of 350 mg/mL was spin coated onto cleaned ITO-coated glass substrates followed by thermal annealing at 70 °C for 10 min. Three tiny dull peaks at 19.6°, 22.86°, and 23.34° exhibited in the XRD pattern of the $PbCl_2$ thin film (Fig. 3.3) match the standard orthorhombic $PbCl_2$ pattern (PDF#74-1803). The weak crystallinity could be attributed to the strong coordination between Pb in $PbCl_2$ and O in DMSO.[41]

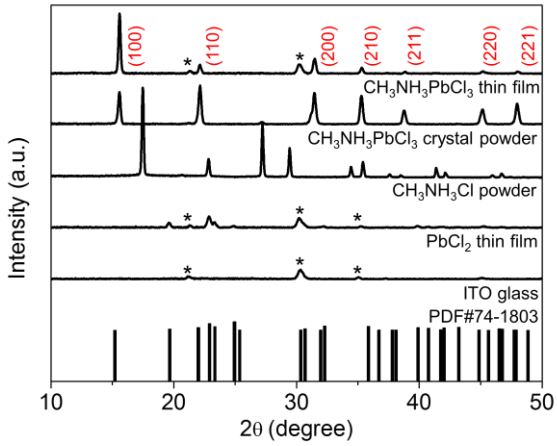

Figure 3.3. XRD patterns of $CH_3NH_3PbCl_3$ thin film on ITO glass, $CH_3NH_3PbCl_3$ crystal powder on glass, CH_3NH_3Cl powder on glass, $PbCl_2$ thin film on ITO glass, ITO glass, and the standard XRD pattern of orthorhombic $PbCl_2$.

SEM images of the $PbCl_2$ film (Figs. 3.4A and B) show densely packed short and long lines with bright contrast and regions with dark contrast. Note that the $PbCl_2$ thin film made in this work exhibited sharper and higher XRD peaks than those of the $PbCl_2$ film fabricated via thermal evaporation.[33] The relatively better crystallinity of our $PbCl_2$ thin films might be the reason that a "harsh" annealing condition was required to fabricate $CH_3NH_3PbCl_3$ thin films as described below compared to the annealing condition (60 °C for 30 min) reported previously.[33] The purity of the

synthesized CH_3NH_3Cl powder was verified by the XRD pattern shown in Fig. 3.3, which is consistent with literature XRD patterns.[42] A CH_3NH_3Cl 2-propanol solution with the concentration of 20 mg/mL was then coated onto the $PbCl_2$ layers and annealed at 70 °C for 30 min to facilitate interdiffusion.

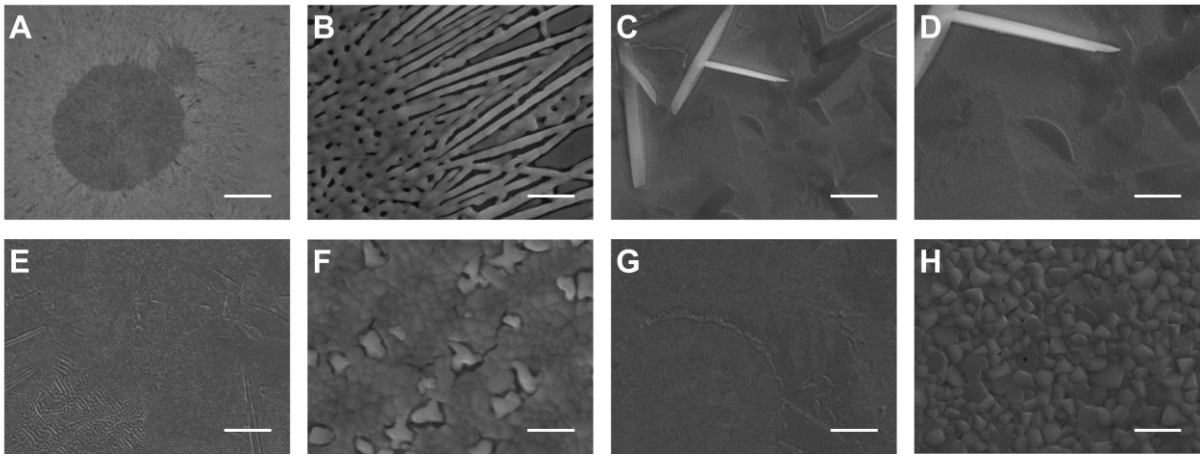

Figure 3.4. (A, B) Top-view SEM images of the $PbCl_2$ thin film annealed at 70 °C for 10 min. (C, D) Top-view SEM images of the $CH_3NH_3PbCl_3$ thin film annealed at 70 °C for 30 min after spin coating CH_3NH_3Cl. (E-H) Top-view SEM images of the final $CH_3NH_3PbCl_3$ thin films after further annealed (E, F) at 100 °C for 1 h and (G, H) DMSO-vapor-assisted thermal annealing at 100 °C for 1 h. Scale bars are 10 μm for A, C, E and G, 5 μm for D and 500 nm for B, F, and H.

As shown in Figs. 3.4C and D, the morphology of the film after the interdiffusion annealing (70 °C for 30 min) showed needle-like, bright ridges. The bright ridges could be attributed to CH_3NH_3Cl, which has a low solubility in 2-propanol and is easily precipitated during the spin coating process. When DMSO-vapor-assisted thermal annealing was introduced at 70 °C for 1 h after the interdiffusion annealing, the needle-like ridges became less bright and sharp (Figs. 3.5A and B). Such changes indicated the improved conductivity of the ridges, the facilitated interdiffusion, and the more complete conversion from CH_3NH_3Cl to $CH_3NH_3PbCl_3$ during this additional DMSO-vapor-assisted thermal annealing. We further increased the temperature of the

additional annealing to 100 °C after the interdiffusion annealing for 1h. The low magnification SEM image of this thermally annealed film (Fig. 3.4E) showed that the continuous film was embedded with many white spots surrounded by cracks. The high magnification SEM image (Fig. 3.4F) clearly showed that the white spots appeared as isolated grains with irregular grain boundaries and gaps, and relatively bright contrast compared to the adjacent grains. The rest of the film was packed with dense, smooth grains with blurry grain boundaries in the size of ~50-200 nm. Another film was annealed at 100 °C with DMSO vapor for 1 h after the interdiffusion annealing. The $CH_3NH_3PbCl_3$ thin film prepared via the DMSO-vapor-assisted thermal annealing exhibited densely packed ~100-400 nm grains with smooth and uniform morphology and clear grain boundaries as shown in both low and high magnification SEM images (Figs. 3.4G and H).

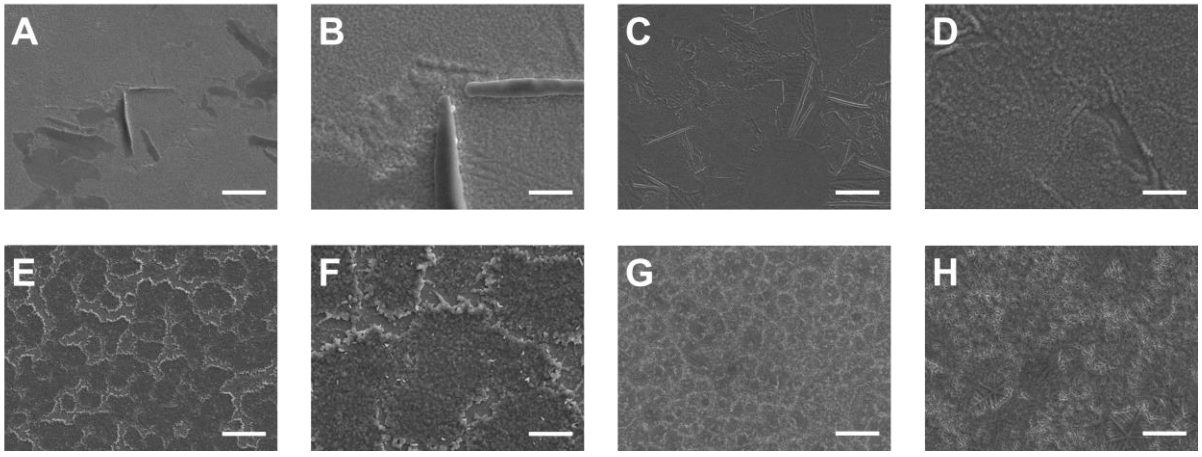

Figure 3.5. (A-F) SEM images of $CH_3NH_3PbCl_3$ thin films made by two-step spin coating under different annealing conditions for each layer. $PbCl_2$ layer was annealed at X °C for 10 min. After spin coating CH_3NH_3Cl, the substrates were annealed at Y °C for 30 min. For DMSO-vapor-assisted thermal annealing, the substrates were annealed at Z °C for 1 h. The values of X, Y, and Z were (A, B) 70, 70 and 70; (C, D) 70, 100 and 100; and (E, F) 100, 100 and 100. Scale bars are 20 μm for A, C, E, and 5 μm for B, D, F. (G,H) SEM images of $PbCl_2$ thin film annealed at 100 °C for 10 min. Scale bars are 20 μm and 5 μm for G and H, respectively.

The quality of $CH_3NH_3PbCl_3$ thin films was found to be sensitive to the temperature of both the $PbCl_2$ annealing and the interdiffusion annealing when the final DMSO-vapor-assisted thermal annealing condition was kept the same as shown in Figs. 3.5C-F. The higher annealing temperature for $PbCl_2$ resulted in better crystallinity of the $PbCl_2$ film (Figs. 3.5G and H), causing a worse morphology of the $CH_3NH_3PbCl_3$ film with broken polycrystalline domains (Figs. 3.5E and F). The best $CH_3NH_3PbCl_3$ thin film was prepared with the $PbCl_2$ annealing at 70 °C for 10 min, the interdiffusion annealing at 70 °C for 30 min, and the DMSO-vapor-assisted thermal annealing at 100 °C for 1 h as shown in Figs. 3.4G and H. This condition was used to prepare $CH_3NH_3PbCl_3$ thin films in the rest of this study.

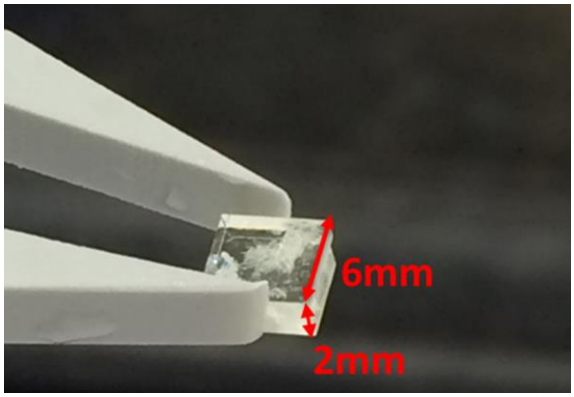

Figure 3.6. Photograph of $CH_3NH_3PbCl_3$ bulk crystal grown via modified inverse temperature crystallization method.

The XRD pattern of the $CH_3NH_3PbCl_3$ thin film made by DMSO-vapor-assisted thermal annealing (Fig. 3.3) showed high purity revealed by the absence of peaks originating from the CH_3NH_3Cl and $PbCl_2$ phases. We also synthesized bulk $CH_3NH_3PbCl_3$ single crystals (6 × 6 × 2 mm, Fig. 3.6) using a modified inverse temperature crystallization method.[31, 43] The XRD pattern of the powder of synthesized single crystals is also shown in Fig. 3.3. All the peaks in the XRD pattern of $CH_3NH_3PbCl_3$ thin film can be found in that of the powder of single crystals. Unlike that each peak (100, 110, 200, 210, 211, 220, and 221) has the similar intensities in the single

crystalline powder XRD pattern, only the peaks at 15.58° (100) and 31.5° (200) dominate in the thin film XRD pattern, indicating that the grains are orientated with the {100} facets parallel to the substrate surface. This agrees well with the flat morphology shown in the SEM images (Figs. 3.4G and H). Strong (100) and (200) peaks were also observed in the XRD pattern of the $CH_3NH_3PbCl_3$ thin films fabricated by the interdiffusion method even though the $PbCl_2$ layer was thermally deposited.[33] The $CH_3NH_3PbCl_3$ thin film with {100} orientated grains could benefit carrier transport and improve vertically structured device performance.

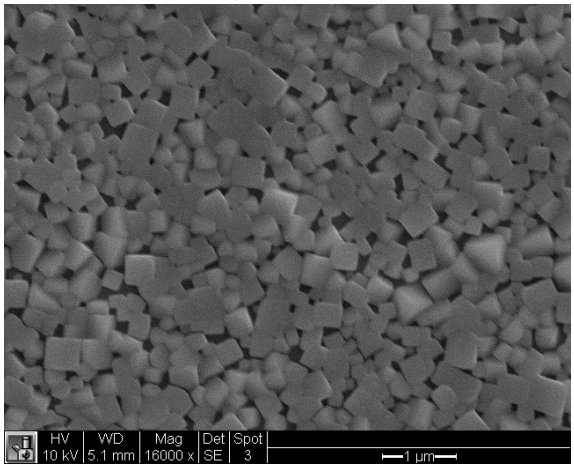

Figure 3.7. SEM image of the $CH_3NH_3PbCl_3$ thin film fabricated with DMSO-vapor-assisted thermal annealing method when the DMSO droplet was too close to the sample

The different morphologies resulted from two annealing processes suggest that thermal annealing under the saturated DMSO vapor environment could facilitate the breaking and reforming of the Pb-Cl bond mediated via DMSO and eventually form the $CH_3NH_3PbCl_3$ thin films with {100} facets dominated larger grains with clear boundaries.[40] Under the super saturation condition, created by adding a DMSO drop too close to the substrate, the thin film went through a more complete recrystallization process resulting in 100-500 nm cubic crystals with identical {100} facets (Fig. 3.7).

3.2 Trap States in Methylammonium Lead Trichloride Thin Film

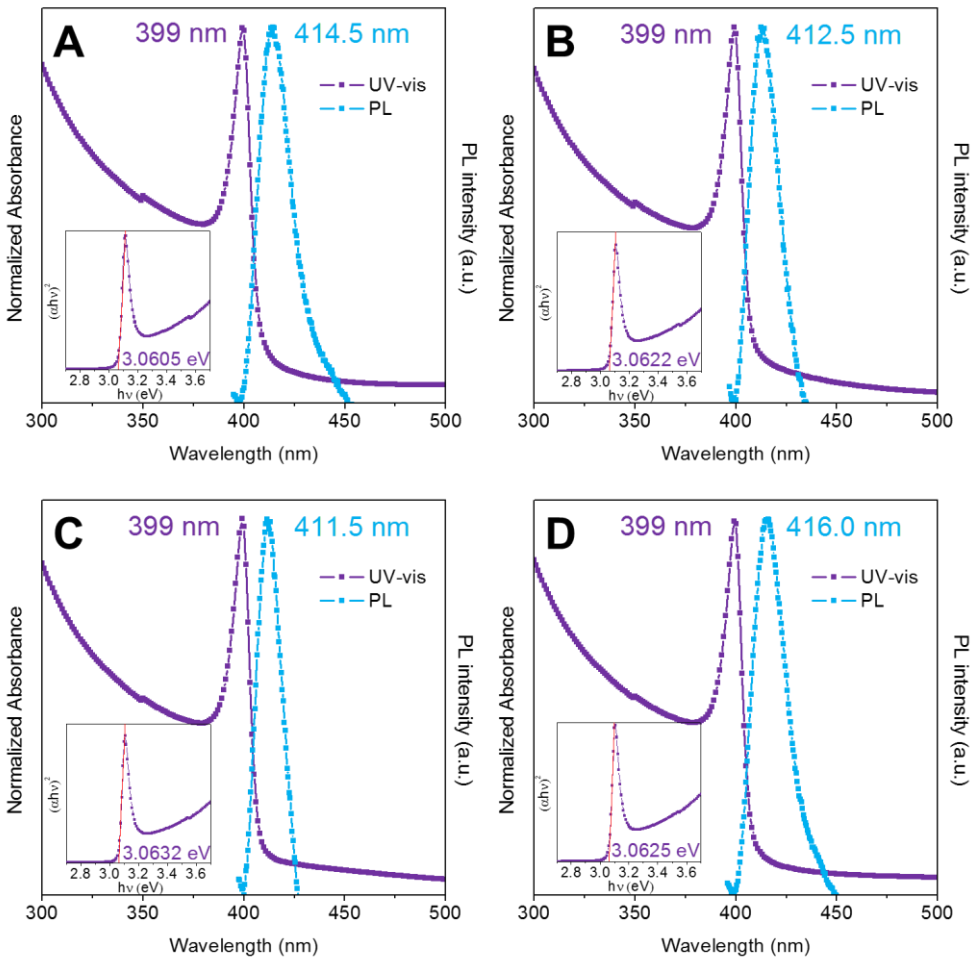

Figure 3.8. Steady-state photoluminescence and absorption spectra of $CH_3NH_3PbCl_3$ thin films fabricated with the $PbCl_2$ DMSO solutions with the concentrations of (A) 250 mg/mL, (B) 300 mg/mL, (C) 350 mg/mL, and (D) 400 mg/mL. The excitation light wavelength is 350 nm. Inset: The optical band gap calculated using the Tauc method.

Molar ratio of two precursors used in the two-step spin coating method is a critical parameter that affects, not only the thickness, but most importantly, the optical and electronic properties of the resulting perovskite thin films, and thus device performance.[44] Therefore, we varied the molar ratio of $PbCl_2$ to CH_3NH_3Cl by changing the concentration of $PbCl_2$ (250, 300, 350 and 400

mg/mL) while maintaining the same CH_3NH_3Cl concentration (20 mg/mL), corresponding to the molar ratios of $PbCl_2$ to CH_3NH_3Cl as 3.03, 3.64, 4.25, and 4.86, respectively. $CH_3NH_3PbCl_3$ perovskite thin films were prepared with these molar ratios using DMSO-vapor-assisted thermal annealing. The average film thicknesses are 97.2, 142.6, 169.3 and 207.4 nm for the $PbCl_2$ concentrations of 250, 300, 350 and 400 mg/mL, respectively. Absorption and steady-state photoluminescence (PL) spectra were acquired from freshly fabricated $CH_3NH_3PbCl_3$ films. As shown in Fig. 3.8, all the four films exhibit a clear absorption cutoff around 405 nm with both excitonic peak and an extended absorption edge representing the continuum of valence-to-conduction band electronic excitations, similar to the reported polycrystalline $CH_3NH_3PbCl_3$ thin films absorption spectra.[11, 12, 33] The optical band gaps were estimated from the Tauc plots for four films and all are around 3.06 eV (Fig. 3.8), close to the previously reported optical band gap of 2.97 eV[11] and ultraviolet photoemission spectroscopy (UPS) determined band gap of 3.17 eV.[12] The strong excitonic peak at band edge was attributed to the more pronounced ionic character in Cl-based perovskites, which leads to a higher exciton binding energy.[12, 33] No excitonic peak was displayed in the $CH_3NH_3PbCl_3$ single crystals and the absorption cutoff was around 430 nm, resulting in an optical band gap of 2.88 eV.[31] As reported previously, lower trap densities, due to higher dimensional structurally coherent units that are tight in the single crystal compared to their polycrystalline counterparts, result in the narrower band gap and the elimination of excitonic peak.[45, 46]

The steady-state PL spectra of the four $CH_3NH_3PbCl_3$ thin films, however, show the shift of emission peaks and different tail lengths. The PL peak blue-shifted from 414.5 nm to 412.5 nm to 411.5 nm when the $PbCl_2$ concentration was increased from 250 mg/mL to 300 mg/mL to 350 mg/mL. Further increasing the $PbCl_2$ concentration to 400 mg/mL red-shifted the PL peak to 416

nm. A clear PL tail extension to 450 nm is shown in Fig. 3.8A for the $CH_3NH_3PbCl_3$ thin film made with 250 mg/mL $PbCl_2$ concentration. With the increase of $PbCl_2$ concentration to 300 mg/mL, the tail was shortened to 430 nm and almost eliminated the tail for the film made with 350 mg/mL $PbCl_2$. The tail extended back to 450 nm when the $PbCl_2$ concentration was increased to 400 mg/mL. Both PL peak shift and tail length change follow the same trend with the concentration of $PbCl_2$. The $CH_3NH_3PbCl_3$ thin film made with the $PbCl_2$ concentration of 350 mg/mL exhibits the shortest wavelength of PL peak and almost no tail following the PL peak, indicating that the film has much less trap states than films made with other $PbCl_2$ concentrations. The formation of trap states in $CH_3NH_3PbI_3$ has been investigated computationally[47-50] and experimentally.[15, 51, 52] Elemental defects derived from Frenkel defects, such as Pb, I, and CH_3NH_3 vacancies, form shallow levels near band edges, which play the role of unintentional doping sources.[47] By investigating the trap states that could be formed by all possible intrinsic point defects in $CH_3NH_3PbI_3$, it was found that Pb vacancies can pull up the valence band and Pb interstitials can pull down the conduction band, which would finally result in a narrower band gap.[48-50] Experimental results showed hole traps at the surface of $CH_3NH_3PbI_3$ thin films and excitonic traps below the optical gaps in these materials, which are likely caused by electron-phonon coupling, especially at surfaces/interfaces of crystalline perovskites.[51] The electron paramagnetic resonance (EPR) studies also showed that in perovskites organic cations that deprotonate from their oxidized state, Pb^{2+} cations as Pb^{3+} centers trap holes while Pb^{2+} cation clusters trap electrons.[52] Pb^{2+} cations were purposely created at the top surface of perovskite films in making vertically stacked photodiode-type photodetectors to achieve high gain through trap-induced photomultiplication.[15] With $PbCl_2$ concentrations 250, 300, or 400 mg/mL, the $CH_3NH_3PbCl_3$ thin films could have more trap states formed either at surfaces, grain

boundaries, or inside grains, leading to red-shift of PL peaks and extended tails. The PL results showed that the $CH_3NH_3PbCl_3$ perovskite thin films fabricated with 350 mg/mL $PbCl_2$ and 20 mg/mL CH_3NH_3Cl had less trap states, providing a control material system to make UV photodetectors.

3.3 UV-A Photodetector Based on Methylammonium Lead Trichloride Thin Film

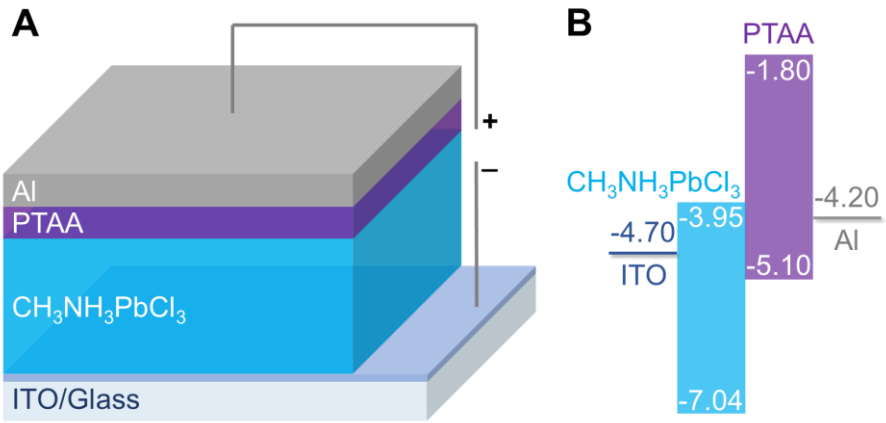

Figure 3.9. (A) Device structure and (B) energy diagram of prototypical visible-blind UV-A photodetector. Energy levels of $CH_3NH_3PbCl_3$ were obtained from polycrystalline thin film.[11]

Motivated by the excellent optical properties of trap-reduced $CH_3NH_3PbCl_3$ thin films, we fabricated prototypical visible-blind UV-A photodetectors with the structure of ITO/$CH_3NH_3PbCl_3$/PTAA/Al (Fig. 3.9A), where ITO serves as cathode, $CH_3NH_3PbCl_3$ thin film (~170 nm) works as the active layer, a visible-blind organic semiconductor PTAA (~35 nm formed by spin coating 10 mg/mL PTAA in toluene) with the band gap of 3.3 eV functions as hole transport/electron blocking layer, and Al (100 nm) serves as anode. The energy diagram of the device is shown in Fig. 3.9B. The valence and conduction energy levels of $CH_3NH_3PbCl_3$ displayed in Fig. 3.9B were adopted from the previous studies determined from $CH_3NH_3PbCl_3$

polycrystalline thin films since polycrystalline thin films were used in our devices and our optical band gap is close to the values reported.[11] Because of the large energy barrier of 2.34 eV between the work function of ITO (-4.70 eV) and the valence band (VB) edge of $CH_3NH_3PbCl_3$ (-7.04 eV), holes would be difficult to inject from ITO cathode to $CH_3NH_3PbCl_3$ under reverse bias. A hole blocking layer can be eliminated. By inserting a PTAA layer between Al anode and $CH_3NH_3PbCl_3$ active layer, it can effectively prevent the electron injection from Al anode to PTAA due to the large energy barrier of 2.40 eV between the work function of Al (-4.20 eV) and the lowest unoccupied molecular orbital (LUMO) of PTAA (-1.80 eV). Therefore, a low dark current was expected. As shown in Fig. 3.10A, the device exhibited a dark current density as low as 1.60×10^{-5} mA/cm^2 under -1 V reverse bias. The dark current density under the same reverse bias is typically in the range of 1×10^{-3} to 2×10^{-6} mA/cm^2 for the previously reported photodiode-type photodetectors based on $CH_3NH_3PbI_3$ with hole/electron blocking layers on each side of the active layer or even double hole or electron blocking layers.[3, 15-18] The low dark current exhibited by our device indicated the good coverage of PTAA, which effectively reduced the electron injection from Al into the high carry mobility perovskite layer under reverse bias. It also demonstrated the high quality of our $CH_3NH_3PbCl_3$ thin films since poor quality films could induce dark current leakage due to the much lower barrier (0.40 eV) for hole injection from ITO to PTAA under reverse bias. The J-V characteristics measured under the illumination of 360 nm monochromatic light with the intensity of 0.267 mW/cm^2 is also shown in Fig. 3.10A, exhibiting a photovoltaic feature with the open circuit voltage (V_{OC}) of 0.92 V. The light current density is 1.41×10^{-2} mA/cm^2 under zero bias, which is about five orders of magnitude higher than the dark current density under the same bias and leads to a photocurrent to dark current ratio, or ON-OFF ratio, to be ~9840 under 0 V bias.

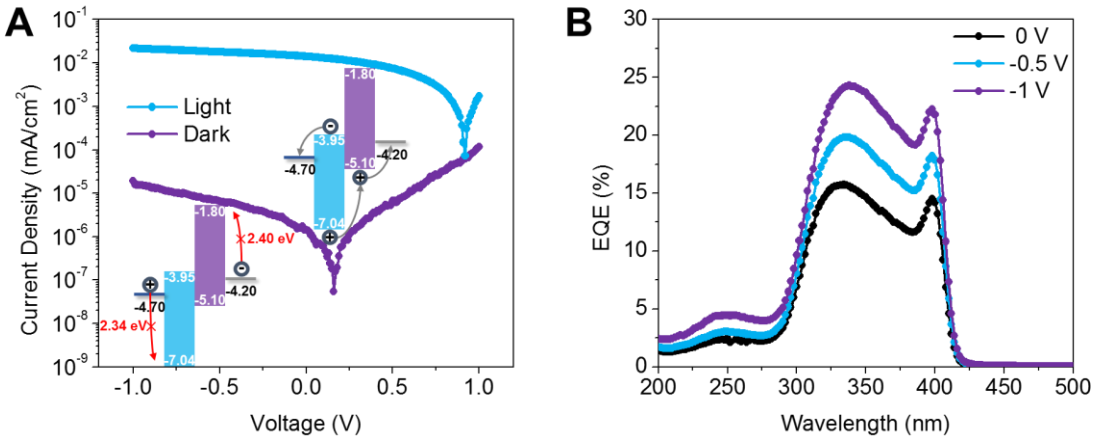

Figure 3.10. (A) Current density-voltage (J-V) characteristics of a prototypical visible-blind UV-A photodetector measured in dark and under 360 nm monochromatic illumination with the intensity of 0.267 mW/cm^2. (B) External quantum efficiency (EQE) of the device versus wavelength under different applied reverse biases.

The external quantum efficiency (EQE) spectra of the device under different applied reverse biases are shown in Fig. 3.10B. The device has a significant photoresponse from 300 to 400 nm with a sharp cutoff at 410 nm. The EQE spectra showed two maxima corresponding to the wavelength of 334 and 398 nm and a dip around 380 nm under 0 V bias. When reverse bias was increased from 0 to -1 V, the first EQE maximum at 334 nm redshifted 4 nm while the wavelength for the second maximum and the dip had no change. The EQE values reached 16% and 15% at 334 and 398 nm, respectively, with no bias, and increased to 24% and 22% under -1 V bias at 338 and 398 nm, respectively, which were much higher than the reported maximum EQEs between 0.2 to 1.6% for narrowband photodetectors based on $CH_3NH_3Pb(Cl\text{-}Br)_3$ and $CH_3NH_3Pb(Br\text{-}I)_3$ single crystals.[32] A reverse bias can facilitate the extraction of carrier generated in the perovskite layer resulting in a higher EQE, which also indicates the carrier extraction is not essentially lossless. For most of the high performance diode type photodetectors based on $CH_3NH_3PbI_3$ polycrystalline thin films, EQE can reach 80% with or without the help of

a low reverse bias,[3, 16-19] and one even reached almost 1 × 10^5% due to photomultiplication via controlling surface traps of $CH_3NH_3PbI_3$ polycrystalline thin films.[15]

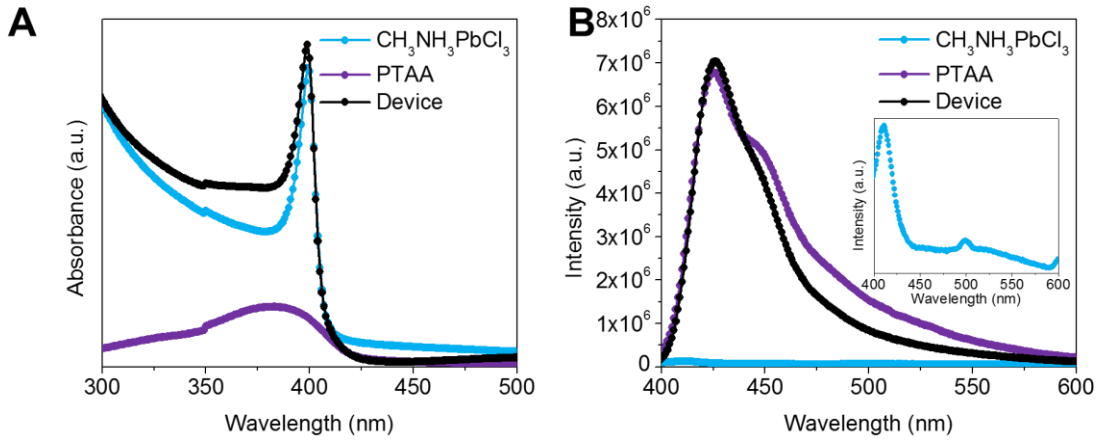

Figure 3.11. (A) Absorption and (B) steady-state PL spectra of $CH_3NH_3PbCl_3$ thin film (~170 nm) on glass, PTAA (~35 nm) on glass, and PTAA (~35 nm) on $CH_3NH_3PbCl_3$ thin film (~170 nm) on glass (i.e., glass/ $CH_3NH_3PbCl_3$/PTAA). The excitation light wavelength is 360 nm.

We investigated the optical properties of single layer $CH_3NH_3PbCl_3$ (~170 nm) and PTAA (~35 nm) and the thin film of PTAA (~35 nm) on $CH_3NH_3PbCl_3$ (~170 nm) as in the devices without two electrodes. The absorption spectra (Fig. 3.11A) showed that both $CH_3NH_3PbCl_3$ and PTAA single films had a sharp optical cut-off at ~410 nm. After coating the PTAA layer on the $CH_3NH_3PbCl_3$ thin film, strong excitonic peak still appeared at the same position as pure $CH_3NH_3PbCl_3$ thin film, and the dip on the left of the excitonic peak was partially filled due to the absorption of PTAA. The absorption spectrum of the film of PTAA on $CH_3NH_3PbCl_3$ is consistent with the photoresponse range of EQE spectra and can help to understand the peaks (~334 and 398 nm) and dip (~380 nm) on EQE spectra. EQE can be expressed by the following equation[53]

$$EQE(\lambda) = \eta_{abs}(\lambda)\eta_{gen}\eta_{coll} \quad (3.1)$$

where η_{abs} is the light absorbance, η_{gen} is the charge carrier generation quantum yield, and η_{coll} is the photo-generated charge carrier collection efficiency. Assuming charge carrier generation quantum yield (η_{gen}) and photo-generated charge carrier collection efficiency (η_{coll}) are the same for different wavelength light in our devices, EQE is only a function of light absorbance (η_{abs}). The peaks and dip of the EQE spectra (Fig. 3.10B) align well with the absorption spectrum of the thin film of PTAA on $CH_3NH_3PbCl_3$ (Fig. 3.11A), indicating that the shape of the EQE spectra mainly determined by the absorbance of the active layer.

Figure 3.11B shows the steady-state PL spectra of the single layer of $CH_3NH_3PbCl_3$ and PTAA and the thin film of PTAA on $CH_3NH_3PbCl_3$ with 360 nm excitation impinged from the sample side. While $CH_3NH_3PbCl_3$ thin film has the similar emission wavelength as that of PTAA thin film, its PL intensity is much weaker even though the $CH_3NH_3PbCl_3$ thin film is almost four times thicker. The PL spectrum of the film of PTAA on $CH_3NH_3PbCl_3$ is dominated by the emission of the thin PTAA with a slightly quenching above 450 nm compared to the PL spectrum of the pure PTAA layer.

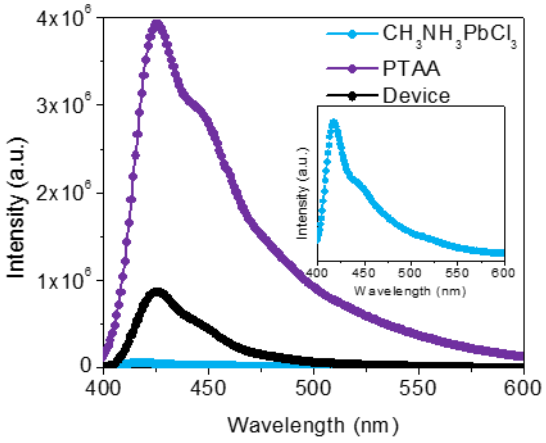

Figure 3.12. Steady-state photoluminescence spectra of $CH_3NH_3PbCl_3$ thin film, pure PTAA thin film, and the film of PTAA on $CH_3NH_3PbCl_3$ excited from glass side with 360 nm wavelength light.

We also impinged the excitation light from the glass side (Fig. 3.12). The PL intensity of the film of PTAA on $CH_3NH_3PbCl_3$ is significantly lower than that of the pure PTAA layer. This is because the thicker $CH_3NH_3PbCl_3$ layer absorbed most of the light but emitted much less light. Therefore, the low EQE in this work could be attributed to the intrinsic poor optoelectronic properties of $CH_3NH_3PbCl_3$ compared to $CH_3NH_3PbI_3$ due to the stronger Pb-Cl interaction. In addition, the large energy offsets at each interface in the device could hinder the carry transport and collection, resulting in lower EQE.

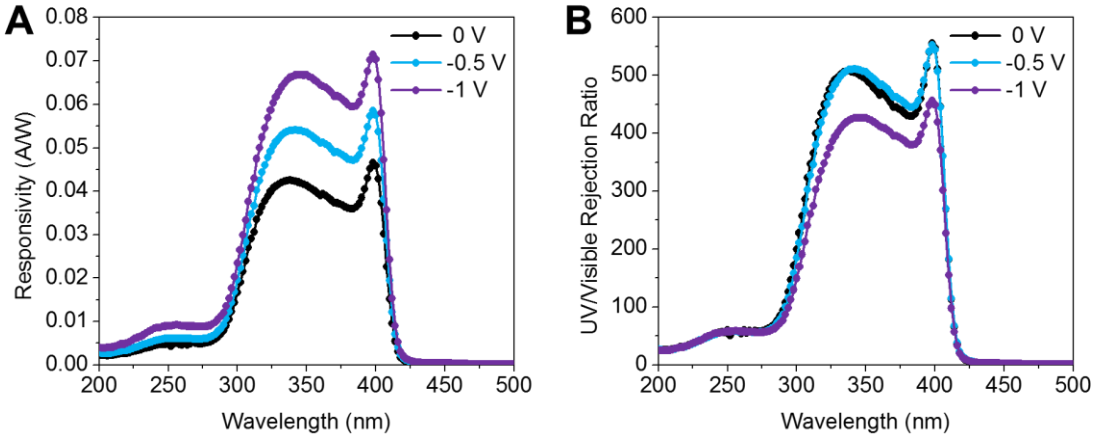

Figure 3.13. (A) Responsivity and (B) UV-visible rejection ratio $R_{UV}/R_{500\ nm}$ of the device versus wavelength under different reverse biases.

We further evaluated the device performance by calculating the responsivity (R), the UV-visible rejection ratio, and the specific detectivity (D*). The responsivity, R, was calculated from EQE according to the following expression

$$R = \frac{EQE \times e}{hv} \tag{3.2}$$

where *e* is the electron charge, *h* is the Planck constant, *v* is the frequency of incident light. The responsivity of the prototypical device reached a maximum of 0.047 A/W and 0.071 A/W at 398 nm under 0 V and -1 V bias, respectively, as shown in Fig. 3.13A. The maximum responsivity of our prototypical device under -1 V bias is almost one fold higher than that (46.9

mA/W) of the photodetector with a $CH_3NH_3PbCl_3$ single crystal sandwiched between a transparent Pt electrode and a Ti/Au back electrode,[31] while it is still significantly lower than the responsivity of 7.56 A/W[32] and 18 A/W[33] of laterally structured phototransistor-type detectors utilizing single crystals. The UV-visible rejection ratio was calculated by $R_{UV}/R_{500\ nm}$ and shown in Fig. 3.13B. Under 0 and -0.5 V biases, UV-visible rejection ratios are similar between 300-400 nm with 508 and 556 at 338 and 398 nm, respectively, which is, to the best of our knowledge, the highest among all the reported UV photodetectors based on $CH_3NH_3PbCl_3$ perovskite.[31-34]

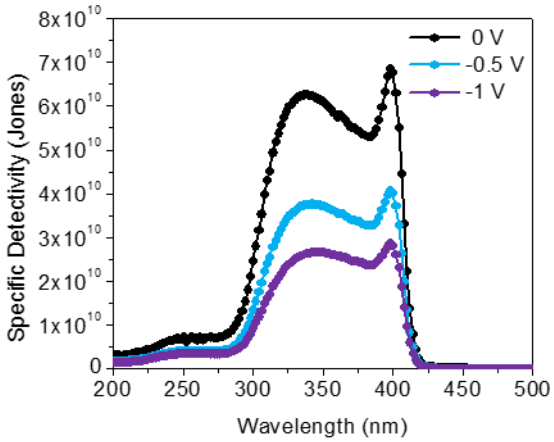

Figure 3.14. Specific detectivity of the device versus wavelength under different reverse biases.

The specific detectivity is given by

$$D^* = \frac{R(A\Delta f)^{\frac{1}{2}}}{i_n} \tag{3.3}$$

where R is the responsivity, A is the device area, Δf is the bandwidth and i_n is the noise current. Assuming that shot noise from the dark current is a major contribution in the total noise current of the photodetector, the specific detectivity was then calculated as

$$D^* = \frac{R}{\sqrt{2eJ_d}} \tag{3.4}$$

where J_d is the dark current density.

Despite the device exhibiting a higher responsivity under -1 V bias, specific detectivity reached a maximum of 6.87×10^{10} Jones at 398 nm under 0 V bias and reduced to 4.07×10^{10} and 2.87×10^{10} Jones under -0.5 V and -1 V bias, respectively, (Fig. 3.14) due to the increased dark current at a higher reverse bias. It also indicates that our prototypical $CH_3NH_3PbCl_3$ visible-blind UV-A photodetecotrs exhibit the best performance when they are self-powered and work at 0 V bias. The detectivity of our device is significantly higher than that of the 350 μm thick single crystal device sandwiched between Pt and Ti/Au electrodes, which is 1.2×10^{10} Jones,[31] while lower than 10^{12} Jones that was achieved by the lateral structured photodetector based on $CH_3NH_3PbCl_3$ homogeneous single crystal.[34]

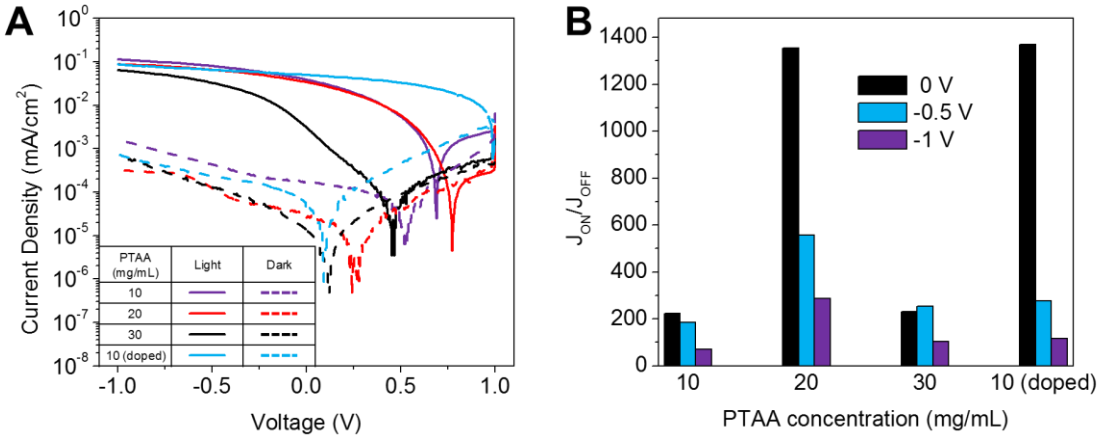

Figure 3.15. (A) J-V characteristics of the devices with the PTAA layer made by 10, 20 and 30 mg/mL PTAA solutions and a 10 mg/mL PTAA solution doped with 1% F4-TCNQ, respectively, under dark and illuminated by a solar simulator with 100 mW/cm^2 intensity. (B) I_{ON}/I_{OFF} ratios of the devices with different PTAA layers.

One of the applications of visible-blind UV-A photodetecotrs is to detect UV-A response when exposed to sunlight. To evaluate the device performance under sunlight and further investigate the effects of PTAA thickness and dopant in PTAA on device performance, we fabricated more devices and tested them using solar simulator. All the devices had $CH_3NH_3PbCl_3$

thin films prepared in the same conditions but the PTAA layers were formed with the concentrations of 10, 20, and 30 mg/mL in order to change the thickness of PTAA layer. F4-TCNQ, which has been reported to have the ability to enhance the solar cell performance by reducing device series resistance,[54] was introduced as a dopant for PTAA. Figure 3.15A shows the J-V curves of the devices tested in dark and under the illumination by solar simulator. With the increase of PTAA layer thickness by spin coating of 10, 20, and 30 mg/mL PTAA solutions, the dark current was reduced from 1.72×10^{-4} to 2.53×10^{-5} and 1.30×10^{-5} mA/cm^2, respectively, under 0 V bias, but reached almost the same under -1 V bias. Similarly, the light current density was decreased under 0 V bias as the PTAA layer was formed by spin coating 30 mg/mL PTAA solution, but reached similar level under -1 V bias. Dopant in PTAA not only decreased dark current density under reverse biases but also increased light current density and V_{OC}, which is consistent with the report for photovoltaic devices.[54] The increased dark current density of the device fabricated with 10 mg/mL PTAA compared to that in Fig. 3.10A could be due to the increased device area from 0.057 cm^2 to 0.1 cm^2 and faster voltage scan speed. We used the ratio of current density measured under the illumination of solar simulator to that in dark, J_{ON}/J_{OFF}, to evaluate the performance of our visible-blind UV-A photodetectors. Figure 3.15B shows the ratio of J_{ON}/J_{OFF} under 0, -0.5 and -1 V biases for the devices made with different PTAA concentrations and with dopant. Device fabricated with F4-TCNQ doped PTAA owned the highest ON-OFF ratio of 1371 at 0 V bias because of its increased light current density and slightly decreased dark current density compared to the device containing the 10 mg/mL PTAA layer without dopant. Following the highest ratio, the device containing the 20 mg/mL PTAA layer showed the second highest ON-OFF ratio of 1354, as both light and dark current densities were decreased. The devices with the 10 and 30 mg/mL PTAA layers suffered

from high dark current density and low light current density, respectively, and thus exhibited relatively low ON-OFF ratios. When the reverse bias was increased to -0.5 V and further -1 V, the ON-OFF ratios of all the four devices decreased due to the significantly increased dark current density and slightly increased light current density.

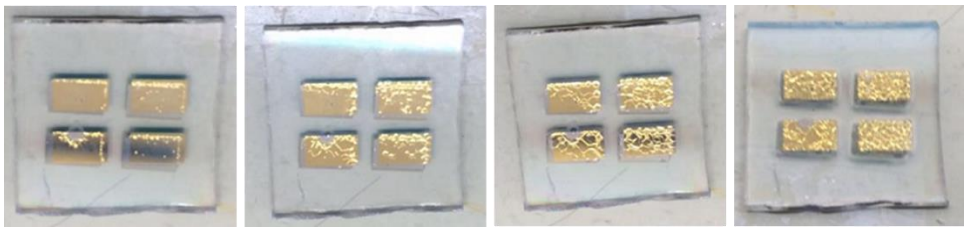

Figure 3.16. Photograph of devices exposed in ambient air (From left to right: 0 min, 1 min, 2 min, 3min)

The environmental instability of perovskite thin films has long been a challenge for the applications in photovoltaic devices.[55] In this study, we also attempted to expose the $CH_3NH_3PbCl_3$ perovskite thin film photodetector devices in ambient air and found that bubbles appeared under the Al electrodes (Fig. 3.16). This phenomenon indicates the degradation of the devices under ambient air and encapsulation is needed in order to conduct the detection in ambient conditions.

Chapter 4. CONCLUSION

In summary, we applied a two-step spin coating and solvent-vapor-assisted low-temperature thermal annealing method to successfully fabricate $CH_3NH_3PbCl_3$ perovskite thin films that exhibited a cubic crystalline structure and pinhole-free morphology. We demonstrated that charge traps in the fabricated $CH_3NH_3PbCl_3$ perovskite thin films could be reduced by carefully adjusting the $PbCl_2$ precursor concentration while keeping the same CH_3NH_3Cl precursor concentration. We further fabricated prototypical UV photodetectors with the structure of ITO/$CH_3NH_3PbCl_3$/PTAA/Al. The devices showed a low dark current density 1.60×10^{-5} mA/cm^2 under -1 V reverse bias, strong photoresponose in 300-400 nm region, and a high UV-visible rejection ratio up to 500 under 0 or -0.5 V bias. The low-temperature solution-processed $CH_3NH_3PbCl_3$ thin films offer a great potential for making flexible, lightweight visible-blind UV-A photodetectors and other optoelectronic devices.

REFERENCES

1. Z. K. Tan, R. S. Moghaddam, M. L. Lai, P. Docampo, R. Higler, F. Deschler, M. Price, A. Sadhanala, L. M. Pazos, D. Credgington, F. Hanusch, T. Bein, H. J. Snaith and R. H. Friend, *Nature Nanotechnology*, 2014, **9**, 687-692.
2. G. R. Li, Z. K. Tan, D. W. Di, M. L. Lai, L. Jiang, J. H. W. Lim, R. H. Friend and N. C. Greenham, *Nano Letters*, 2015, **15**, 2640-2644.
3. L. T. Dou, Y. Yang, J. B. You, Z. R. Hong, W. H. Chang and G. Li, *Nature Communications*, 2014, **5**, 6.
4. NREL Efficiency chart, https://www.nrel.gov/pv/assets/images/efficiency-chart.png).
5. Q. Q. Lin, A. Armin, R. C. R. Nagiri, P. L. Burn and P. Meredith, *Nature Photonics*, 2015, **9**, 106-112.
6. M. A. Green, A. Ho-Baillie and H. J. Snaith, *Nature Photonics*, 2014, **8**, 506-514.
7. G. C. Xing, N. Mathews, S. Y. Sun, S. S. Lim, Y. M. Lam, M. Gratzel, S. Mhaisalkar and T. C. Sum, *Science*, 2013, **342**, 344-347.
8. C. Wehrenfennig, G. E. Eperon, M. B. Johnston, H. J. Snaith and L. M. Herz, *Advanced Materials*, 2014, **26**, 1584-1589.
9. Z. G. Xiao, C. Bi, Y. C. Shao, Q. F. Dong, Q. Wang, Y. B. Yuan, C. G. Wang, Y. L. Gao and J. S. Huang, *Energy & Environmental Science*, 2014, **7**, 2619-2623.
10. F. Hao, C. C. Stoumpos, R. P. H. Chang and M. G. Kanatzidis, *Journal of the American Chemical Society*, 2014, **136**, 8094-8099.
11. C. Li, J. Wei, M. Sato, H. Koike, Z. Z. Xie, Y. Q. Li, K. Kanai, S. Kera, N. Ueno and J. X. Tang, *Acs Applied Materials & Interfaces*, 2016, **8**, 11526-11531.

12. R. Comin, G. Walters, E. S. Thibau, O. Voznyy, Z. H. Lu and E. H. Sargent, *Journal of Materials Chemistry C*, 2015, **3**, 8839-8843.

13. Y. Yuan, R. Xu, H. T. Xu, F. Hong, F. Xu and L. J. Wang, *Chinese Physics B*, 2015, **24**, 5.

14. K. T. Butler, J. M. Frost and A. Walsh, *Materials Horizons*, 2015, **2**, 228-231.

15. R. Dong, Y. J. Fang, J. Chae, J. Dai, Z. G. Xiao, Q. F. Dong, Y. B. Yuan, A. Centrone, X. C. Zeng and J. S. Huang, *Advanced Materials*, 2015, **27**, 1912-+.

16. Q. Q. Lin, A. Armin, D. M. Lyons, P. L. Burn and P. Meredith, *Advanced Materials*, 2015, **27**, 2060-2064.

17. Y. J. Fang and J. S. Huang, *Advanced Materials*, 2015, **27**, 2804-+.

18. C. Liu, K. Wang, C. Yi, X. J. Shi, P. C. Du, A. W. Smith, A. Karim and X. Gong, *Journal of Materials Chemistry C*, 2015, **3**, 6600-6606.

19. D. Li, G. F. Dong, W. Z. Li and L. D. Wang, *Scientific Reports*, 2015, **5**, 6.

20. B. R. Sutherland, A. K. Johnston, A. H. Ip, J. X. Xu, V. Adinolfi, P. Kanjanaboos and E. H. Sargent, *Acs Photonics*, 2015, **2**, 1117-1123.

21. Y. L. Guo, C. Liu, H. Tanaka and E. Nakamura, *Journal of Physical Chemistry Letters*, 2015, **6**, 535-539.

22. H. Deng, D. D. Dong, K. K. Qiao, L. L. Bu, B. Li, D. Yang, H. E. Wang, Y. B. Cheng, Z. X. Zhao, J. Tanga and H. S. Song, *Nanoscale*, 2015, **7**, 4163-4170.

23. X. Hu, X. D. Zhang, L. Liang, J. Bao, S. Li, W. L. Yang and Y. Xie, *Advanced Functional Materials*, 2014, **24**, 7373-7380.

24. K. Domanski, W. Tress, T. Moehl, M. Saliba, M. K. Nazeeruddin and M. Gratzel, *Advanced Functional Materials*, 2015, **25**, 6936-6947.

25. Y. Zhang, J. Du, X. H. Wu, G. Q. Zhang, Y. L. Chu, D. P. Liu, Y. X. Zhao, Z. Q. Liang and J. Huang, *Acs Applied Materials & Interfaces*, 2015, **7**, 21634-21638.

26. S. F. Zhuo, J. F. Zhang, Y. M. Shi, Y. Huang and B. Zhang, *Angewandte Chemie-International Edition*, 2015, **54**, 5693-5696.

27. H. R. Xia, J. Li, W. T. Sun and L. M. Peng, *Chemical Communications*, 2014, **50**, 13695-13697.

28. E. Horvath, M. Spina, Z. Szekrenyes, K. Kamaras, R. Gaal, D. Gachet and L. Forro, *Nano Letters*, 2014, **14**, 6761-6766.

29. L. W. Sang, M. Y. Liao and M. Sumiya, *Sensors*, 2013, **13**, 10482-10518.

30. E. Monroy, F. Omnes and F. Calle, *Semiconductor Science and Technology*, 2003, **18**, R33-R51.

31. G. Maculan, A. D. Sheikh, A. L. Abdelhady, M. I. Saidaminov, M. A. Hague, B. Murali, E. Alarousu, O. F. Mohammed, T. Wu and O. M. Bakr, *Journal of Physical Chemistry Letters*, 2015, **6**, 3781-3786.

32. Y. J. Fang, Q. F. Dong, Y. C. Shao, Y. B. Yuan and J. S. Huang, *Nature Photonics*, 2015, **9**, 679-+.

33. W. Z. Wang, H. T. Xu, J. Cai, J. B. Zhu, C. W. Ni, F. Hong, Z. B. Fang, F. Z. Xu, S. W. Cui, R. Xu, L. J. Wang, F. Xu and J. Huang, *Optics Express*, 2016, **24**, 8411-8419.

34. V. Adinolfi, O. Ouellette, M. I. Saidaminov, G. Walters, A. L. Abdelhady, O. M. Bakr and E. H. Sargent, *Advanced Materials*, 2016, **28**, 7264-+.

35. P. Docampo, J. M. Ball, M. Darwich, G. E. Eperon and H. J. Snaith, *Nature Communications*, 2013, **4**, 6.

36. G. E. Eperon, V. M. Burlakov, P. Docampo, A. Goriely and H. J. Snaith, *Advanced Functional Materials*, 2014, **24**, 151-157.

37. Q. Wang, Y. C. Shao, Q. F. Dong, Z. G. Xiao, Y. B. Yuan and J. S. Huang, *Energy & Environmental Science*, 2014, **7**, 2359-2365.

38. H. C. Cho, S. H. Jeong, M. H. Park, Y. H. Kim, C. Wolf, C. L. Lee, J. H. Heo, A. Sadhanala, N. Myoung, S. Yoo, S. H. Im, R. H. Friend and T. W. Lee, *Science*, 2015, **350**, 1222-1225.

39. Z. G. Xiao, Q. F. Dong, C. Bi, Y. C. Shao, Y. B. Yuan and J. S. Huang, *Advanced Materials*, 2014, **26**, 6503-6509.

40. L. Z. Zhu, B. Yuh, S. Schoen, X. P. Li, M. Aldighaithir, B. J. Richardson, A. Alamer and Q. M. Yu, *Nanoscale*, 2016, **8**, 7621-7630.

41. G. W. Warren and H. Henein, *Hydrometallurgy*, 1997, **46**, 243-247.

42. E. L. Unger, A. R. Bowring, C. J. Tassone, V. L. Pool, A. Gold-Parker, R. Cheacharoen, K. H. Stone, E. T. Hoke, M. F. Toney and M. D. McGehee, *Chemistry of Materials*, 2014, **26**, 7158-7165.

43. M. I. Saidaminov, A. L. Abdelhady, B. Murali, E. Alarousu, V. M. Burlakov, W. Peng, I. Dursun, L. F. Wang, Y. He, G. Maculan, A. Goriely, T. Wu, O. F. Mohammed and O. M. Bakr, *Nature Communications*, 2015, **6**, 6.

44. Q. Wang, Y. C. Shao, H. P. Xie, L. Lyu, X. L. Liu, Y. L. Gao and J. S. Huang, *Applied Physics Letters*, 2014, **105**, 5.

45. Q. F. Dong, Y. J. Fang, Y. C. Shao, P. Mulligan, J. Qiu, L. Cao and J. S. Huang, *Science*, 2015, **347**, 967-970.

46. M. I. Saidaminov, A. L. Abdelhady, G. Maculan and O. M. Bakr, *Chemical Communications*, 2015, **51**, 17658-17661.

47. J. Kim, S. H. Lee, J. H. Lee and K. H. Hong, *Journal of Physical Chemistry Letters*, 2014, **5**, 1312-1317.

48. W. J. Yin, T. T. Shi and Y. F. Yan, *Applied Physics Letters*, 2014, **104**, 4.

49. W. J. Yin, T. T. Shi and Y. F. Yan, *Advanced Materials*, 2014, **26**, 4653-+.

50. W. J. Yin, T. T. Shi and Y. F. Yan, *Journal of Physical Chemistry C*, 2015, **119**, 5253-5264.

51. X. X. Wu, M. T. Trinh, D. Niesner, H. M. Zhu, Z. Norman, J. S. Owen, O. Yaffe, B. J. Kudisch and X. Y. Zhu, *Journal of the American Chemical Society*, 2015, **137**, 2089-2096.

52. I. A. Shkrob and T. W. Marin, *Journal of Physical Chemistry Letters*, 2014, **5**, 1066-1071.

53. A. Armin, Y. L. Zhang, P. L. Burn, P. Meredith and A. Pivrikas, *Nature Materials*, 2013, **12**, 593-593.

54. Q. Wang, C. Bi and J. S. Huang, *Nano Energy*, 2015, **15**, 275-280.

55. D. Wang, M. Wright, N. K. Elumalai and A. Uddin, *Solar Energy Materials and Solar Cells*, 2016, **147**, 255-275.